Research Article | Vol. 13, No. 7 / 1 Jul 2023 / Optical Materials Express 2120

Optical Materials EXPRESS

High frequency characterization of PZT thin-films deposited by chemical solution deposition on SOI for integrated high speed electro-optic modulators

GILLES F. FEUTMBA,[1,2,3,†] LEANDRO DA SILVA,[4,†] NISHANT SINGH,[4] LAURENS BREYNE,[5] KOBE DE GEEST,[1,2,3] JOHN PUTHENPARAMPIL GEORGE,[1,3] JOHAN BAUWELINCK,[4] DRIES VAN THOURHOUT,[2,3] XIN YIN,[4] AND JEROEN BEECKMAN[1,3,*]

[1] *Liquid Crystals and Photonics Group, ELIS Department, Ghent University, Technologiepark-Zwijnaarde, Gent 9052, Belgium*
[2] *Photonics Research Group, INTEC Department, Ghent University-imec, Technologiepark-Zwijnaarde, Gent 9052, Belgium*
[3] *Center for Nano- and Biophotonics (NB-Photonics), Ghent University, Technologiepark-Zwijnaarde, Gent 9052, Belgium*
[4] *IDLab, Ghent University–imec, Technologiepark-Zwijnaarde, Gent 9052, Belgium*
[5] *IDLab, Ghent University–imec, Technologiepark-Zwijnaarde, Gent 9052 Belgium. Currently at Nokia Bell labs, Antwerp, Belgium*
[†] These authors contributed equally to this work as co-first authors
[*] *jeroen.beeckman@ugent.be*

Abstract: The increasing demand for high data rates and low power consumption puts silicon photonics at the edge of its capabilities. The heterogeneous integration of optical ferro-electric materials on silicon enhances the functionality of the silicon on insulator (SOI) platform to meet these demands. Lead zirconate titanate (PZT) thin films with a large Pockels coefficient and good optical quality can be directly integrated on SOI waveguides for fast electro-optic modulators. In this work, the relative permittivity and dielectric loss of PZT thin films deposited by chemical solution deposition on SOI substrates are analyzed at high frequencies. We extract $\varepsilon_r = 1650 - 2129$ and $\tan(\delta) = 0.170 - 0.209$ for the PZT thin films in the frequency range 1-67GHz. We show the possibility of achieving bandwidths beyond 60GHz via a Mach-Zehnder modulator with $V_\pi = 7$V, suitable for next generation data communication systems.

1. Introduction

Silicon (Si) photonics has emerged as a key enabling technology in the 21st century, leveraging the long existing CMOS infrastructure and the high index contrast of the SOI (silicon-on-insulator) platform. Compact and scalable low-loss passive and active devices, mass-manufactured at a low cost, have been demonstrated on the platform [1–4]. Si photonics integrated circuits are seen as the catalyzers for the next generation technology for different application domains such as sensing [5], medical diagnosis [6], and quantum information processing [7]. The huge demand for higher data rates and lower power consumption for high performance computing and data communication has been the main drive of Si photonics research.

Si modulators, mainly exploiting plasma dispersion effects are limited in bandwidth by carrier recombination lifetime, have high insertion loss and suffer from residual amplitude modulation i.e. the change of the refractive index of the waveguide is directly coupled with a change in absorption [3,8,9].

#494148 https://doi.org/10.1364/OME.494148
Journal © 2023 Received 27 Apr 2023; revised 20 Jun 2023; accepted 20 Jun 2023; published 29 Jun 2023

Optical Materials EXPRESS

Electro-optic (EO) modulation based on the Pockels effect is an efficient way of obtaining near lossless and ultra-fast modulators for next generation data communication systems. However the Pockels effect is absent in Si due to its centrosymmetric structure, and breaking the crystal symmetry by applying strain using silicon nitride (SiN) films results in a very small Pockels coefficient [10]. The integration of EO materials exhibiting the Pockels effect has therefore been pursued as a viable alternative for ultra-fast and low loss modulators in SOI platform. EO polymers have been integrated in slotted waveguides for Si-organic hybrid modulators with low $V_\pi L$ [11]. Low-loss lithium niobate ($LiNbO_3$) waveguides and highly crystalline barium titanate ($BaTiO_3$) thin films have been integrated on Si and have demonstrated high speed modulation [12,13]. While organic materials suffer from instability, $LiNbO_3$ and $BaTiO_3$ based modulators require complex processing and expensive bonding.

Lead zirconate titanate (PZT) films have been widely used as transducers in electronics and they possess a higher Pockels coefficient than $LiNbO_3$ (conventionally used for long-haul communication). Recently, a thin-film crystal EO on insulator Mach-Zehnder modulator (MZM) with PZT waveguides was proposed in [14]. The PZT film was grown by chemical solution deposition (CSD) on top of a SiO_2/Si substrate, and the ridge waveguides were fabricated by photolithography and inductively coupled plasma (ICP) etching. The obtained Pockels coefficient of 96pm/V with a modulation efficiency $V_\pi L$ = 1.4V.cm at 1550nm wavelength provided a bandwidth of 12GHz with 5mm long MZM. Estimating the PZT $\varepsilon_r = 700$, the authors propose that velocity matching should allow a bandwidth above 50GHz, thus further increase of the bandwidth would be possible with the optimization of the CPW structure.

We use a novel approach to integrate strongly electro-optic thin films of PZT on Si using a thin and transparent intermediate lanthanide-based layer as a seed for PZT growth as opposed to the conventionally used Pt-based seed layers, enabling direct growth of the thin PZT film on top of Si waveguides, i.e. without bonding [15]. PZT thin films are deposited by CSD and the films show strong ferro-electricity with an open electrical hysteresis signature [15]. The potential of the technology for next generation high speed systems has been demonstrated by the development of low-loss hybrid PZT-SiN electro-optic modulators with bias-free operation and high bandwidth (beyond 30GHz) on a SiN platform [16].

To achieve high speed modulation using PZT thin films directly grown on a SOI platform, knowledge of the dielectric constant (ε_r) and the dielectric loss ($\tan(\delta)$) at microwave frequencies is a prerequisite for proper electrodes design. J. George et al. measured $\varepsilon_r \approx 650$ and $\tan(\delta) \approx 0.038$ from PZT thin films grown on glass substrates using a capacitive measurement, with the PZT ferroelectric domains poled out-of-plane [15]. Similarly, T. Van de Veire et al. measured $\varepsilon_r \approx$ 400-2000 from PZT thin films with different thicknesses and the ferroelectric domains poled in-plane [17]. The results are comparable with values obtained from PZT ceramics and thin films grown using different techniques on metallic based substrates [18,19]. The results were however limited to low frequencies. To properly assess the potential of PZT thin-films, their high-frequency properties have to be evaluated, in a process similar to what [20] performed for $BaTiO_3$ thin-films. As shown in [19], the loss tangent of PZT can change dramatically as the excitation frequency surpasses 1GHz.

In this work, the relative permittivity and dielectric loss of PZT thin films deposited by CSD on SOI substrates are analyzed at microwave frequencies using coplanar waveguide (CPW) transmission lines (TL). We have fabricated multiple CPWs of different lengths and gap sizes on three samples with different PZT thicknesses. The CPWs are characterized using S-parameter measurements and the permittivity ε_r and loss tangent $\tan(\delta)$ of the PZT are extracted. By comparing experimental and simulation results of the S-parameters, we could extract $\varepsilon_r = 1650 - 2129$ and $\tan(\delta) = 0.170 - 0.209$ for the PZT thin films in the frequency range 1-67GHz. We then show an optimized electrode design for achieving bandwidths beyond 60GHz

Optical Materials EXPRESS

for a PZT electro-optic modulator on SOI, suitable for next generation data communication systems.

2. Sample fabrication and methods

PZT thin films are grown on a SOI substrate by CSD using a lanthanide-based intermediate layer [15]. The intermediate layer acts both as a barrier layer to prevent the diffusion of lead (Pb) and as a seed layer for PZT growth. The SOI substrate comprises a 220nm thick device silicon layer and a 2µm thick buried oxide layer. A 10nm thick lanthanide-based intermediate layer is then deposited followed by the PZT thin film deposition.

The PZT thin films are deposited by a repeated spin-coating and annealing process which allows control of the film thickness. Thicker PZT thin films can therefore be obtained by multiple spincoating and annealing steps. We use the chemical composition $PbZr_{0.52}Ti_{0.48}O_3$ for our PZT thin film, which is at the morphotropic phase boundary. The PZT layer is deposited and annealed at 600°C for 15 minutes in a tube furnace under an oxygen ambient. RF coplanar waveguides (CPW) are then fabricated on top of the PZT thin film using photolithography, thermal evaporation and lift-off. A stack of 10nm thick Titanium (Ti) layer and 650nm thick gold (Au) layer is used as metal. The CPWs have a width of 30µm for both ground and signal lines. Transmission lines with lengths of 2mm, 3mm and 4mm and gap sizes of 3µm, 4µm and 5µm were fabricated and used for the analysis. The CPWs were fabricated on three different samples with PZT thicknesses of 112.9nm (S1), 186.9nm (S2) and 255.7nm (S3) (measured via SEM on a cross section). Thicker PZT thin films are prone to defects [21], which could potentially deteriorate the film's properties.

Figure 1(a) and 1(b) show the top view and the SEM cross-section of the CPW structure used to characterize the RF properties of the PZT thin films. Figure 1(c) shows the schematic of the measurement set-up used to measure the CPWs' S-parameters. Ground-signal-ground GSG-50A RF probes are used to make the electrical contacts. The microwave network analyzer N5247B PNA-X from Keysight is used. The RF probes are calibrated using a CS-100 substrate with a short-open-load-through (SOLT) measurement. CPWs with the same lengths, widths and gaps are fabricated directly on the SOI substrate and the S-parameters are measured as a reference for the substrate dielectric and metal losses.

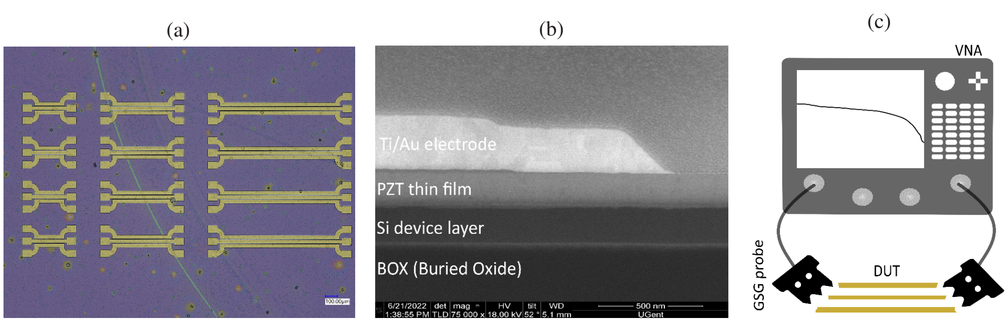

Fig. 1. (a) Top view of different RF coplanar waveguide structures used for RF characterization. Ti/Au electrodes are evaporated on PZT thin films grown on SOI substrates. (b) Scanning electron microscope (SEM) image of the coplanar waveguide structure. (c) Setup used for the RF measurements. The device under test (DUT) is probed by two ground-signal-ground (GSG) probes connected to a vector network analyzer (VNA).

After growth, the PZT thin film is polycrystalline with the ferroelectric domains preferentially oriented along the (100) plane and a random in-plane orientation imposed by the lanthanide-based seed layer as shown in previous publications [15,21]. The PZT thin film is poled to align the

Optical Materials EXPRESS

ferroelectric domains in-plane, in a configuration that allows for obtaining significant electro-optic response for a quasi-TE optical mode. The PZT thin film is poled at room temperature after the patterning of CPWs. The PZT film across the CPW is poled for a push-pull configuration; i.e., the ferroelectric domains are aligned in the same direction across the CPWs for a modulating field in opposite direction across the CPW. For this, a voltage divider is used to apply an equal electric field in the same direction across the CPWs. The PZT thin film is poled by applying an asymmetric block wave across the CPW. Firstly, 10V/µm is applied across the different CPWs for ten minutes, followed by a reversed field of -1V/µm for one minute. These steps are repeated for an hour. The rectangular waveform is to prevent electric field charge accumulation at the PZT/metallic interface. S-parameters measurements were obtained for both poled and unpoled samples.

3. Results and discussion

Figure 2 shows the microwave attenuation, effective dielectric constant, and characteristic impedance of the different CPWs for poled and unpoled samples. These transmission line parameters were obtained from the measured S parameters by using Eqs. (1).

$$Z_0 = \sqrt{\frac{Z_{11}}{Y_{11}}} \tag{1a}$$

$$\Gamma = \frac{1}{L} \cdot \operatorname{arctanh}\left(\frac{1}{Z_0 \cdot Y_{11}}\right) \tag{1b}$$

$$\alpha = \mathrm{Re}(\Gamma) \tag{1c}$$

$$\beta = \mathrm{Im}(\Gamma) \tag{1d}$$

$$\varepsilon_{\mathrm{e}} = \left(\frac{c\beta}{\omega}\right)^2 \tag{1e}$$

where Z_0 is the characteristic impedance, Z_{11} and Y_{11} are the first elements of the Z and Y parameters obtained from the S parameters, Γ is the reflection coefficient, L is the CPW length, α is the attenuation constant, β is the phase constant, ε_{e} is the effective relative permittivity, c is the speed of light in free space, and ω is the angular frequency of the microwave signal.

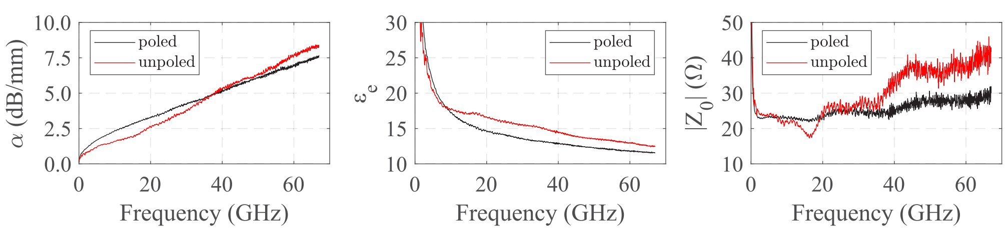

Fig. 2. Propagation loss, effective relative permittivity, and characteristic impedance for poled and unpoled samples. Both set of traces are for a 112.9nm thick PZT layer (S1), 4µm gap and 2mm length transmission lines.

We observe a variation in the properties obtained from the unpoled samples compared to the poled samples. The impedance of the poled samples is more uniform, with no appreciable change across the measurement bandwidth. Propagation losses tend to be smaller for poled samples at frequencies above 30GHz. Poled samples present lower effective permittivity ε_{e} than unpoled ones for frequencies above 5 to 20GHz. Similar trends were observed for the other samples with different PZT thicknesses, gap sizes and transmission line lengths. These differences observed

Optical Materials EXPRESS

between poled and unpoled samples could be attributed to the ferroelectric domains orientation and interaction. After growth, the ferroelectric domains have a random in-plane and out-of-plane orientation while the poled samples have the ferroelectric domains aligned in-plane along the poling field, and parallel to the direction of the applied RF field during measurements. At high frequencies, the randomness in the orientation of the ferroelectric domains and the domain wall interactions could lead to a large variation in the properties of the thin film.

Figure 3 shows that the impedance of the CPW increases with the gap size, facilitating the matching to 50Ω drivers. A larger gap size also decreases the propagation loss and effective permittivity, improving velocity matching between optical and RF waves, and ultimately leading to a higher modulation bandwidth. A similar trend is observed when reducing the PZT layer thickness, as shown in Fig. 4, i.e., a smaller PZT thickness leads to higher impedance, lower propagation loss and smaller effective permittivity, enabling a higher modulation bandwidth.

Figure 5 shows the general trends for the CPW parameters at the frequency of 50GHz, as the PZT thickness and gap size changes.

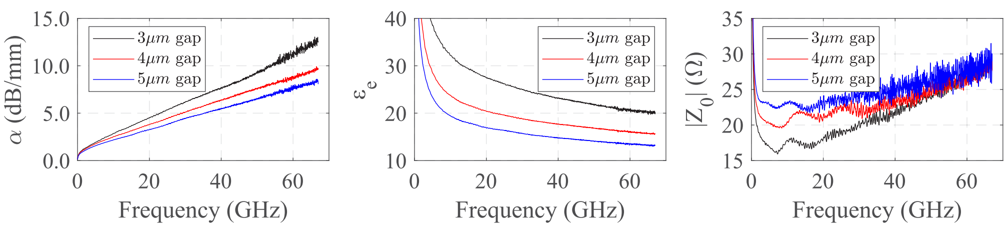

Fig. 3. Properties of the samples for different electrode gap sizes. All three samples are for 3 spin-coated layers of PZT (thickness of 186.9nm).

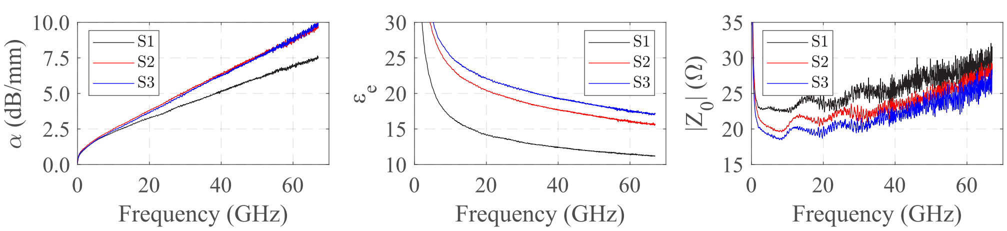

Fig. 4. Properties of the samples for different PZT spin-coated layers. All three samples are for a CPW length of 3mm and electrode gap of 4μm.

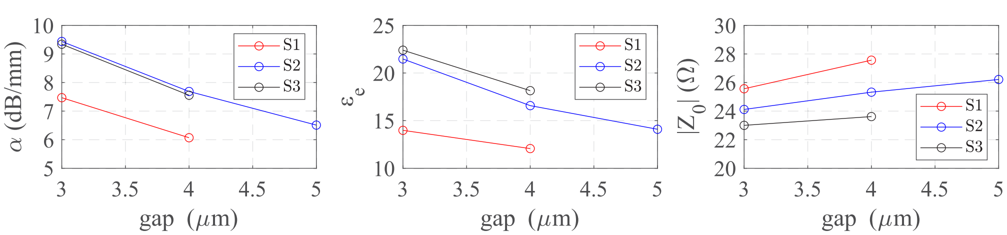

Fig. 5. CPW parameters trends at 50GHz for different gap sizes and PZT thickness.

Increasing the gap size and reducing the PZT thickness enables a higher modulation bandwidth, however this also leads to a lower modulation efficiency (high $V_\pi L$), which for a push-pull driven modulator is given by Eq. (2a). The lower efficiency is due to the fact that an increase in the

Optical Materials EXPRESS

gap size reduces the electric field and the fact that the gap size and PZT thickness influences the overlap between the microwave and optical fields. The factor 2 in the denominator accounts for the equal but opposite phase changes in the two arms of an MZM modulator [22,23].

$$V_\pi L = \frac{g}{\Gamma_o} \cdot \left(\frac{\lambda_0}{2 \cdot r_{33} \cdot n_{pzt}^3} \right) \tag{2a}$$

$$\Gamma_o = \frac{g}{V_o} \frac{\int E_m \cdot |E_{opt}^2| ds}{\int |E_{opt}^2| ds} \tag{2b}$$

where V_π is the half-wave voltage (i.e. the required voltage to change the relative phase between the two MZM arms by π radians [24]), g is the gap size, λ_o is the optical wavelength in vacuum, r_{33} is the linear electro-optical coefficient which is dominant in this configuration, n_{pzt} is the optical refractive index of the PZT thin film, Γ_o is the overlap integral, V_o is the voltage that generates the microwave electrical field E_m, and E_{opt} is the optical electrical field.

Figure 6 shows Lumerical Mode simulation results when the silicon waveguides are 240nm wide. The second factor in the right hand side of Eq. (2a) is constant for a given optical material and optical wavelength, thus the modulation efficiency $V_\pi L$ is a function of the gap size g and the overlap integral Γ_o. By using the data from Fig. 6(a), it is possible to estimate the modulation efficiency according to Eq. (2a), as shown in Fig. 6(b).

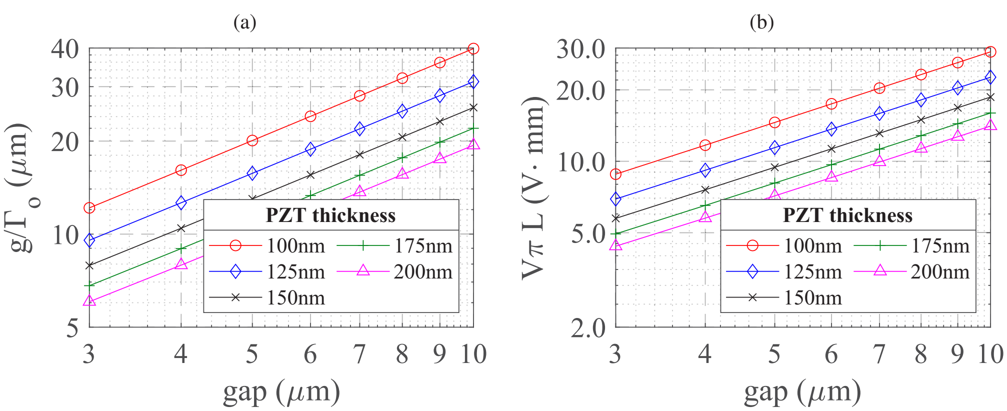

Fig. 6. Lumerical Mode simulation showing the effect of gap size and PZT thickness on the (a) g/Γ_o and (b) $V_\pi L$ values. For $V_\pi L$ calculation, $\lambda_0 = 1.55\mu$m, $n_{pzt} = 2.48$ and $r_{33} = 70$ pm/V were used.

3.1. Extraction of PZT permittivity (ε) and loss tangent ($\tan(\delta)$)

Simulations by Keysight PathWave Advanced Design System (ADS) have been carried out using the method of moments (MoM) in microwave mode, as the problem is planar in nature. The simulation was setup with the same material stack as the measured CPWs (Fig. 7) to reproduce the effective response of the CPWs and extract the relative permittivity and dielectric loss of the PZT thin film. The low-resistivity silicon substrate was chosen due to its lower cost. This may, however, affect RF loss and reduce modulator bandwidth. In ADS the material permittivity is modeled according to the Svensson-Djordevic model [25,26]. The CPW traces are modeled as 3D-distributed, with the domain meshed at the frequency of 70GHz, minimum of 40 cells per wavelength, edge meshing of 5 μm and at least 4 cells in the width of each CPW trace.

Figure 8 shows the values of α, ε_e, and Z_0 for the 7 measured samples and the simulation results from ADS. For each simulation different values of permittivity and loss tangent were

Optical Materials EXPRESS

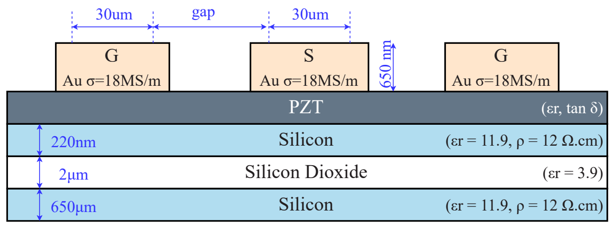

Fig. 7. Cross section view of the substrate used for the simulations.

chosen for the PZT layer to achieve the best individual fit, according to Table 1. Ideally all fitted permittivity and loss tangent values would be the same, however due to the extremely thin PZT layer, the simulated transmission line parameters are relatively insensitive to changes on PZT permittivity. The loss tangent average is 0.1921, with a standard deviation of 0.0115, while the relative permittivity average is 1902 with a standard deviation of 146. In the frequency-dependent Svensson-Djordevic model the loss tangent is specified for a frequency of 1GHz, with a low frequency of 1kHz and high frequency of 1THz.

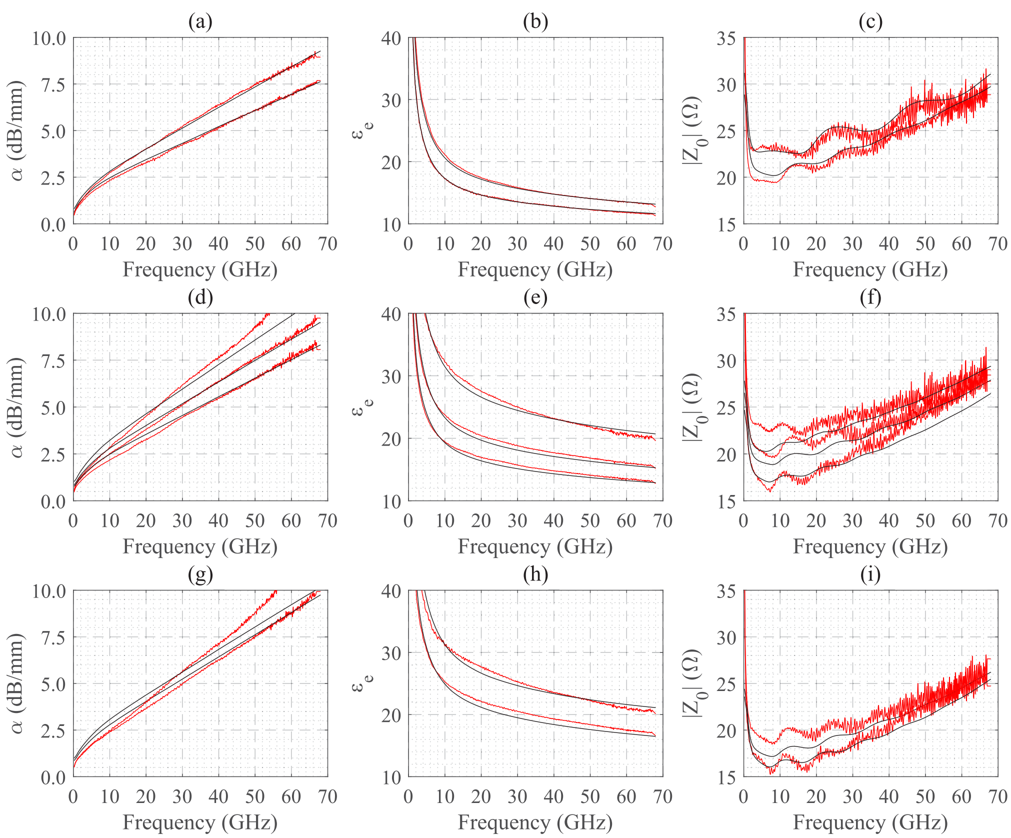

Fig. 8. Keysight ADS simulations (black traces) and measurements (red traces). Sub-figures show α, ε_e and $|Z_0|$ for (a-c) 112.9nm, (d-f) 186.9nm, and (g-i) 255.7nm PZT thicknesses.

Table 1. Fitted values for the permittivity and loss tangent of PZT thin-film

PZT thickness	Gap	PZT relative permittivity	PZT loss tangent
112.9nm (S1)	3µm	2128.86	0.209486
112.9nm (S1)	4µm	1961.33	0.198218
186.9nm (S2)	3µm	2008.53	0.184599
186.9nm (S2)	4µm	1913.32	0.197493
186.9nm (S2)	5µm	1890.86	0.195395
255.7nm (S3)	3µm	1650.01	0.169982
255.7nm (S3)	4µm	1763.79	0.189316

3.2. Mach-Zehnder modulator design

In order to appreciate the properties of the PZT material for electro-optical modulation, this section presents a discussion on the design of a MZM using the proposed PZT thin-films.

Figure 9(a) shows the optical mode profile for the quasi-TE mode of a hybrid PZT/Si optical waveguide and the electric field lines distribution from the side electrodes. The cross-section of the hybrid PZT/Si optical waveguide shows a 200nm thick PZT thin film on a Si waveguide 240nm wide and 220nm thick, with electrodes 4µm apart. The simulated electro-optic confinement factor in the PZT thin film for this cross-section is 0.503 and there is negligible metallic absorption loss. This cross-section is chosen from an optimization study performed for hybrid PZT-Si electro-optic modulators [27]. The optical group index of the hybrid PZT/Si waveguide (n_{og}) is obtained via simulation in Lumerical MODE and shown in Fig. 9(b). Information on the expected optical losses arising from the PZT film can be found in the Supplement 1, measured in waveguide geometry (fig. S1) and via spectroscopic ellipsometry (fig. S2). The measured AFM rms roughness of the PZT film is 1.582 nm (see fig. S3).

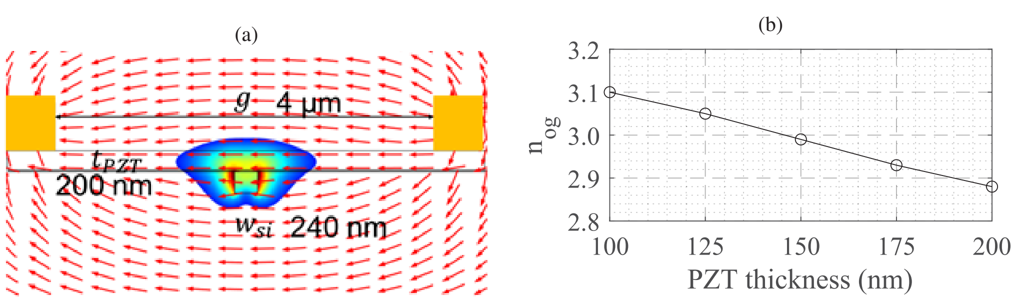

Fig. 9. Lumerical MODE simulation showing (a) the optical mode and (b) the change of hybrid mode optical group index with PZT layer thickness.

Assuming negligible microwave propagation losses, the velocity mismatch limited 3dB electrical bandwidth of the modulator (equivalent to the 6dB optical bandwidth) would be estimated by [28]:

$$BW = \frac{1.39c}{\pi L(n_m - n_{og})} \tag{3}$$

Where c is the speed of light, L is the modulation length, and n_m is the effective microwave index. Considering that the effective permittivity considerably changes with frequency due to dispersion, the bandwidth has to be evaluated for the value of permittivity at the bandwidth frequency:

$$n_m = \sqrt{\varepsilon_e(BW)} \tag{4}$$

Optical Materials EXPRESS

As shown in Fig. 10 for the measured samples, velocity matching between optical and microwave waves allows for a bandwidth higher than 75GHz. However, as previously shown in Fig. 8, microwave propagation loss is not negligible, and must be taken into account to estimate the bandwidth.

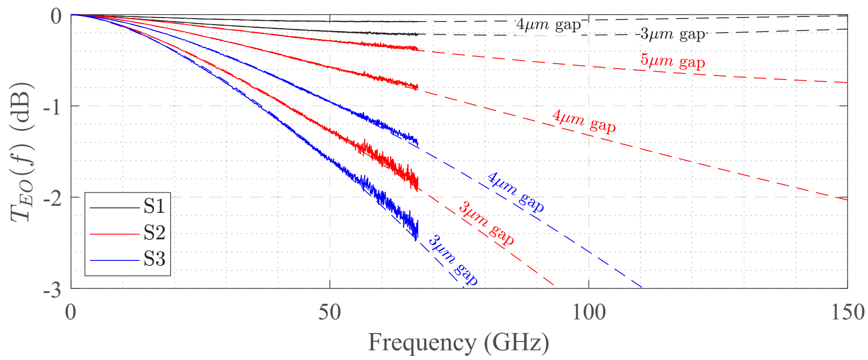

Fig. 10. Normalized 1mm length bandwidth with microwave propagation losses neglected. Hybrid PZT/Si optical group index is taken from Fig. 9(b). Dashed lines are extrapolations.

Conductor and dielectric losses are the main contributors to the microwave propagation losses. Taking the extracted propagation losses into account, the normalized small-signal electro-optic frequency response [28] can be calculated as shown in Eq. (5).

$$T_{EO}(f) = e^{-\frac{\alpha L}{2}} \sqrt{\frac{\sinh^2\left(\frac{\alpha L}{2}\right) + \sin^2\left(\frac{\xi L}{2}\right)}{\left(\frac{\alpha L}{2}\right)^2 + \left(\frac{\xi L}{2}\right)^2}} \tag{5}$$

where L is the modulation length, α is the attenuation coefficient, f is the microwave frequency and ξ is a velocity mismatch parameter given by:

$$\xi = \frac{2\pi f(n_m - n_{og})}{c} \tag{6}$$

By taking propagation losses into account, the estimated normalized bandwidth per mm length for the samples drops to values between 25 and 52GHz, as shown in Fig. 11.

To better understand the relative contributions originating from microwave propagation loss and phase velocity mismatch on the bandwidth, Fig. 12 shows the estimated frequency response of the 4μm gap CPW from sample S1 and the 3μm gap CPW from sample S3 (respectively the samples with the highest and lowest expected bandwidth) with either propagation losses or phase velocity mismatch neglected. It clearly shows that a reduction in propagation losses has a more pronounced effect on bandwidth than velocity matching, which means that microwave losses have to be more closely examined.

The microwave losses can be further broken down into conduction and dielectric losses, as depicted in Fig. 13. The red traces are the measured sample, while the black traces are the simulation. The blue traces are the simulation when a perfect conductor is used for the electrodes (thus it represents dielectric loss), and the dashed green trace is the difference between the total loss and the loss with the perfect conductor, and it represents the conduction loss only. As can be seen from the α traces, dielectric loss is more relevant than conduction loss for higher frequencies. It may also be seen from the imaginary part of the characteristic impedance, as a

Optical Materials EXPRESS

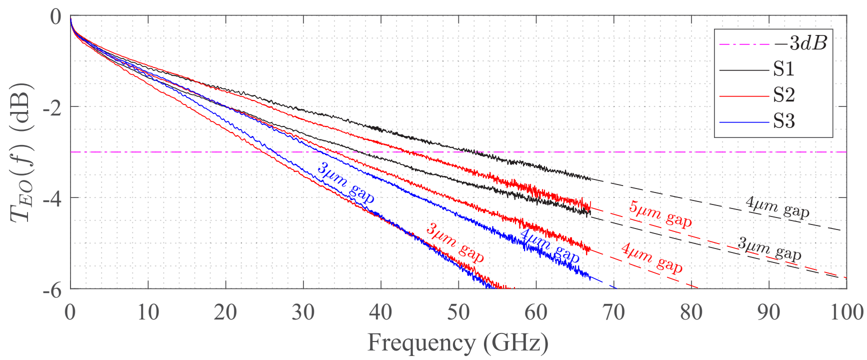

Fig. 11. Frequency response taking both velocity mismatch and propagation loss into account. Extrapolation is shown as dashed lines. All graphs are normalized for a modulation length of 1mm.

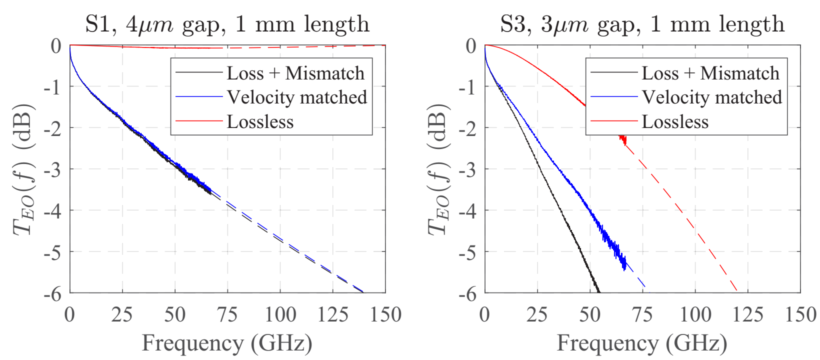

Fig. 12. Frequency response when either microwave loss or velocity mismatch is neglected. Graphs are normalized for a modulation length of 1mm.

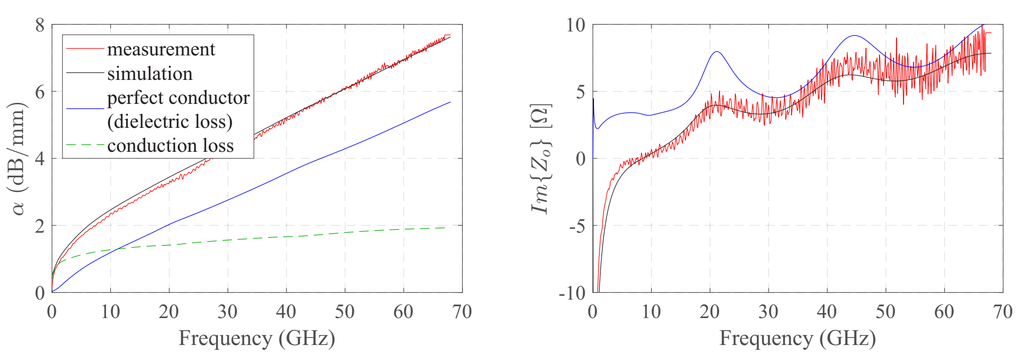

Fig. 13. Loss breakdown between conductor and dielectric. Red traces are the measured sample (S1, 4μm gap), black traces are the simulation, blue traces are the simulation with perfect conductors for the electrodes, and the green dashed trace is the difference between total loss and dielectric loss.

Optical Materials EXPRESS

positive imaginary impedance represents predominantly dielectric loss [29]. We can also notice that the dielectric contributes more than twice the conductor for the total loss at 50GHz.

Using Eqs. (2a) and (5), the trade-off between modulation efficiency and bandwidth for the measured samples is presented in Fig. 14. Each trace represents a PZT thickness and gap size, when the modulator length is swept between 0.5mm (circle marker) and 2.0mm (triangle marker). When designing a MZM the goal is to maximize bandwidth while minimizing the half-wave voltage, which translates into moving from the bottom-right to the top-left region of the graph.

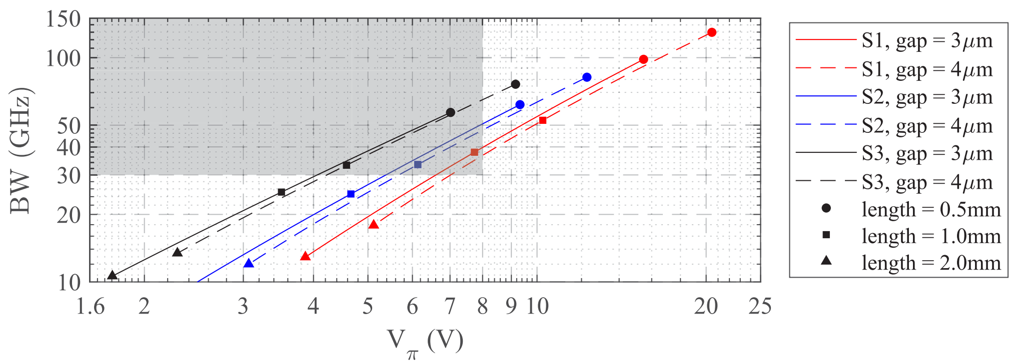

Fig. 14. Trade-off between modulation efficiency and bandwidth. Longer modulators reduce the V_π requirement, but also lead to a lower 3dB electro-optical bandwidth. A narrower electrode gap helps to reduce the necessary modulator length for the same performance. A thicker PZT layer with a narrower gap is preferable to improve the trade-off between modulation efficiency and bandwidth. The shaded region represents the constraints for the example design.

Thus, even if a thin PZT layer with a wide gap leads to a higher achievable bandwidth for the same modulator length (as previously shown in Fig. 11), it is always possible to use a thicker PZT layer with a narrower gap and a shorter modulator length to achieve a better trade-off between modulator efficiency and bandwidth. A shorter length also translates into a smaller footprint, saving chip real-state.

As an example design, we consider a CMOS driven PAM-4 electro-optical modulator biased at the quadrature point for 56Gbaud transmission. A CMOS driver is normally capable of delivering an output voltage swing of 2Vpp at most [30]. The theoretical extinction ratio (ER) for the MZM can be calculated as:

$$ER = 10 \cdot \log_{10}\left[\frac{1+\cos\left[\frac{\pi}{2}\left(1-\frac{V_d}{V_\pi}\right)\right]}{1+\cos\left[\frac{\pi}{2}\left(1+\frac{V_d}{V_\pi}\right)\right]}\right] \tag{7}$$

where V_d is the peak-to-peak driver voltage swing.

The 400GBASE-DR4 requires a minimum extinction ratio of 3.5dB, which means $V_\pi \leq 4V_d$. For a CMOS driver, this constraint limits the maximum half-wave voltage to be $V_\pi \leq 8V$.

On the other hand, to achieve 56GBaud, a bandwidth of at least 30GHz is normally required [31]. The shaded region in Fig. 14 shows the constraints for the example design.

We can now investigate the effect of changing electrode width and thickness on the estimated performance of the modulator. As a reference, we choose S3 (255.7nm thick PZT layer) with 3μm gap.

Figure 15 shows CPW α, ε_e, Z_0, and the $V_\pi \times BW$ trade-off for different electrode widths using a momentum simulation. For the simulation both signal and ground traces had the same width.

Optical Materials EXPRESS

As shown in the figure, increasing the electrode width leads to a reduced propagation loss and lower effective permittivity, but it also leads to a lower characteristic impedance requiring a lower output impedance driver. It may also be noticed that the benefit of increasing the electrode width is less pronounced when the width is larger (that is, there are diminishing returns).

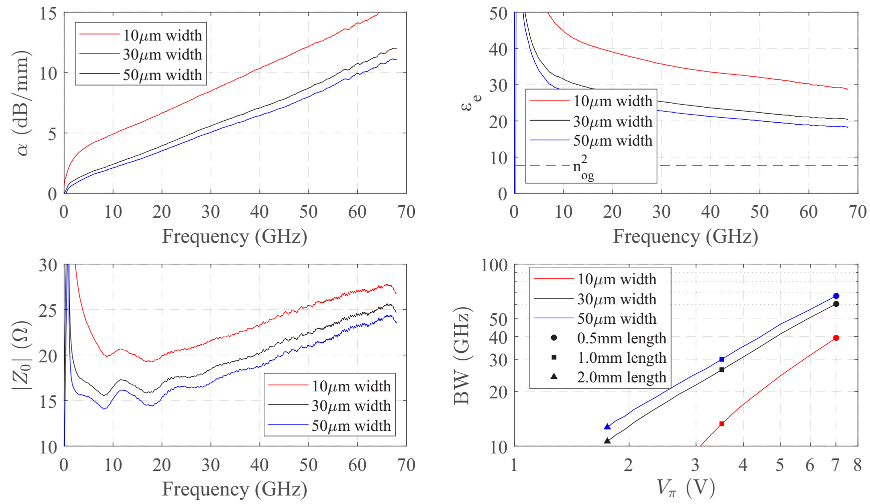

Fig. 15. Effect of changing the electrodes width on the estimated performance of the modulator. The black trace represents the S3 (255.7nm thick PZT layer) with 3μm gap. Results were obtained with ADS momentum simulation, by using the measured sample values and the offsets from simulations.

Figure 16 shows the effect of increasing the electrodes thicknesses on the CPW α, ε_e, Z_0 and the $V_\pi \times BW$ trade-off. As can be seen, increasing the thickness of the electrodes has the same effect as increasing their width. However, it should be noted that increasing the width is normally easier and less expensive than increasing the thickness. Also, increasing either the width/thickness or increasing the gap/reducing the PZT layer thickness both can decrease α, ε_e, and Z_0 of the CPW. But contrary to increasing the gap or reducing the PZT layer thickness, increasing the electrodes width or thickness lead to an improvement of the trade-off $V_\pi \times BW$, because they do not directly affect the overlap integral.

The dashed magenta traces in both Fig. 15 and Fig. 16 represent the square of the hybrid optical mode index for S3 (255.7nm PZT thickness). The distance from this trace and the permittivity traces represent the amount of velocity mismatch between the optical and microwave waves. As can be seen, it is difficult to achieve velocity matching without increasing the electrodes width or thickness excessively, and thus reducing the characteristic impedance and degrading the electrical matching between the driver and the modulator.

From both Fig. 15 and Fig. 16 we have shown that a modulator based on the presented PZT thin-film process has the potential to reach bandwidths beyond 60GHz, while having a half-wave voltage <7V, for a modulator length of around 0.5mm.

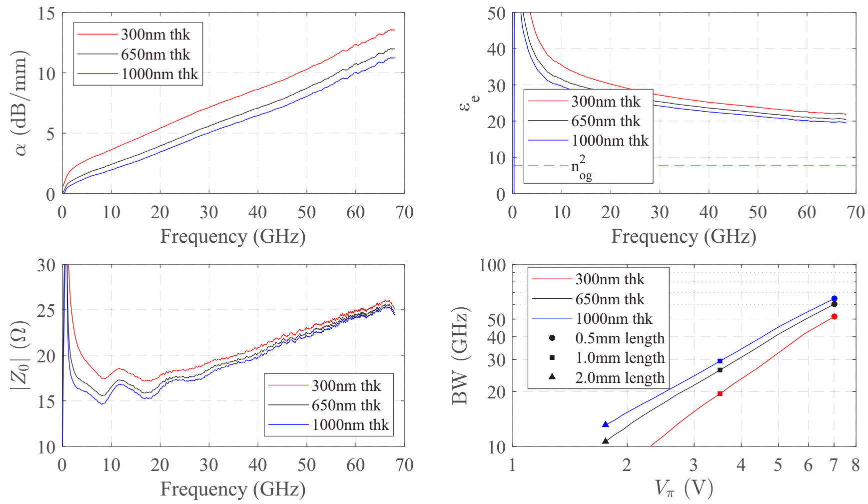

Fig. 16. Effect of changing the electrodes thickness on the estimated performance of the modulator. The black trace represents the S3 (255.7nm thick PZT layer) with 3μm gap. Results were obtained with ADS momentum simulation, by using the measured sample values and the offsets from simulations.

4. Conclusions

The relative permittivity and dielectric loss of PZT thin films deposited by chemical solution deposition on SOI substrates have been extracted for frequencies up to 67GHz. A thin and low-loss lanthanide layer is used as the seed layer for the PZT thin films growth and allows for direct integration over Si waveguides for electro-optic modulation. The RF characteristics were then obtained from the fabricated PZT thin films.

By comparing experimental and simulation results of the S-parameters from fabricated transmission lines, we could extract $\varepsilon_r = 1650 - 2129$ and $\tan(\delta) = 0.170 - 0.209$ for the PZT thin-films in the frequency range 1-67GHz.

Next we have demonstrated the trade-offs for the design of a Mach-Zehnder modulator in a hybrid PZT/Si device for a TE optical mode. Modulation bandwidths above 60GHz with $V_\pi \approx 7V$ are projected taking into account microwave propagation losses. This positions PZT thin film as a promising candidate, with a simple CSD deposition process, for next generation data communication modulators on the SOI platform.

Funding. Fonds Wetenschappelijk Onderzoek (1S68218N).

Acknowledgments. Gilles Freddy Feutmba acknowledges support and funding as an SB-PhD Fellow of the research foundation–Flanders (FWO, grant number 1S68218N). We thank Ewout Picavet for providing the AFM results.

Disclosures. The authors declare no conflicts of interest.

Data availability. Data underlying the results presented in this paper are not publicly available at this time but may be obtained from the authors upon reasonable request.

Supplemental document. See Supplement 1 for supporting content.

References

1. R. Soref, "The past, present, and future of silicon photonics," IEEE J. Sel. Top. Quantum Electron. **12**(6), 1678–1687 (2006).
2. P. Dumon, W. Bogaerts, V. Wiaux, J. Wouters, S. Beckx, J. Van Campenhout, D. Taillaert, B. Luyssaert, P. Bienstman, D. Van Thourhout, and R. Baets, "Low-loss SOI photonic wires and ring resonators fabricated with deep UV lithography," IEEE Photonics Technol. Lett. **16**(5), 1328–1330 (2004).

3. G. T. Reed, G. Mashanovich, F. Y. Gardes, and D. J. Thomson, "Silicon optical modulators," Nat. Photonics **4**(8), 518–526 (2010).
4. J. Michel, J. Liu, and L. C. Kimerling, "High-performance Ge-on-Si photodetectors," Nat. Photonics **4**(8), 527–534 (2010).
5. D. Kohler, G. Schindler, L. Hahn, J. Milvich, A. Hofmann, K. Länge, W. Freude, and C. Koos, "Biophotonic sensors with integrated Si_3N_4-organic hybrid (SiNOH) lasers for point-of-care diagnostics," Light: Sci. Appl. **10**(1), 64 (2021).
6. A. Li, C. Yao, J. Xia, H. Wang, Q. Cheng, R. Penty, Y. Fainman, and S. Pan, "Advances in cost-effective integrated spectrometers," Light: Sci. Appl. **11**(1), 174 (2022).
7. E. Pelucchi, G. Fagas, I. Aharonovich, D. Englund, E. Figueroa, Q. Gong, H. Hannes, J. Liu, C.-Y. Lu, N. Matsuda, J.-W. Pan, F. Schreck, F. Sciarrino, C. Silberhorn, J. Wang, and K. D. Jöns, "The potential and global outlook of integrated photonics for quantum technologies," Nat. Rev. Phys. **4**(3), 194–208 (2021).
8. R. Soref and B. Bennett, "Electrooptical effects in silicon," IEEE J. Quantum Electron. **23**(1), 123–129 (1987).
9. G. T. Reed, G. Z. Mashanovich, F. Y. Gardes, M. Nedeljkovic, Y. Hu, D. J. Thomson, K. Li, P. R. Wilson, S.-W. Chen, and S. S. Hsu, "Recent breakthroughs in carrier depletion based silicon optical modulators," Nanophotonics **3**(4-5), 229–245 (2014).
10. C. Lafforgue, M. Berciano, L. Deniel, G. Marcaud, X. L. Roux, C. A. Ramos, D. Benedikovic, V. Vakarin, A. Ruiz-Caridad, P. Crozat, D. Marris-Morini, E. Cassan, and L. Vivien, "High-speed optical modulation based on Pockels effect in strained silicon waveguides," in *Conference on Lasers and Electro-Optics*, (2020), p. SM2J.1.
11. S. Wolf, H. Zwickel, W. Hartmann, M. Lauermann, Y. Kutuvantavida, C. Kieninger, L. Altenhain, R. Schmid, J. Luo, A. K.-Y. Jen, S. Randel, W. Freude, and C. Koos, "Silicon-organic hybrid (SOH) Mach-Zehnder modulators for 100 Gbit/s on-off keying," Sci. Rep. **8**(1), 2598 (2018).
12. N. Boynton, H. Cai, M. Gehl, S. Arterburn, C. Dallo, A. Pomerene, A. Starbuck, D. Hood, D. C. Trotter, T. Friedmann, C. T. DeRose, and A. Lentine, "A heterogeneously integrated silicon photonic/lithium niobate travelling wave electro-optic modulator," Opt. Express **28**(2), 1868–1884 (2020).
13. F. Eltes, C. Mai, D. Caimi, M. Kroh, Y. Popoff, G. Winzer, D. Petousi, S. Lischke, J. E. Ortmann, L. Czornomaz, L. Zimmermann, J. Fompeyrine, and S. Abel, "A $BaTiO_3$ -based electro-optic pockels modulator monolithically integrated on an advanced silicon photonics platform," J. Lightwave Technol. **37**(5), 1456–1462 (2019).
14. D. Ban, G. Liu, H. Yu, Y. Wu, and F. Qiu, "Low driving voltage and low optical loss electro-optic modulators based on lead zirconate titanate thin film on silicon substrate," J. Lightwave Technol. **40**(9), 2939–2943 (2022).
15. J. P. George, P. F. Smet, J. Botterman, V. Bliznuk, W. Woestenborghs, D. Van Thourhout, K. Neyts, and J. Beeckman, "Lanthanide-assisted deposition of strongly electro-optic PZT thin films on silicon: toward integrated active nanophotonic devices," ACS Appl. Mater. Interfaces **7**(24), 13350–13359 (2015).
16. K. Alexander, J. P. George, J. Verbist, K. Neyts, B. Kuyken, D. Van Thourhout, and J. Beeckman, "Nanophotonic Pockels modulators on a silicon nitride platform," Nat. Commun. **9**(1), 3444 (2018).
17. T. Van de Veire, J. P. George, H. Rijckaert, K. Neyts, J. Lauwaert, F. Beunis, and J. Beeckman, "In-plane characterization of PZT thin films for the creation of a general impedance model," J. Appl. Phys. **129**(9), 094501 (2021).
18. M. D. Nguyen, R. J. A. Steenwelle, P. M. te Riele, J. M. Dekkers, D. H. A. Blank, and G. Rijnders, "Ferroelectric and dielectric properties of $Pb(Zr,Ti)O_3$ thin film capacitors," in *2009 4th IEEE International Conference on Nano/Micro Engineered and Molecular Systems*, (2009), pp. 649–652.
19. H.-J. Zhao, T.-L. Ren, N.-X. Zhang, R.-Z. Zuo, X.-H. Wang, L.-T. Liu, Z.-J. Li, Z.-L. Gui, and L.-T. Li, "High-frequency properties of PZT for RF-communication applications," Mater. Sci. Eng. B **99**(1-3), 192–194 (2003).
20. A. Rosa, D. Tulli, P. Castera, A. M. Gutierrez, A. Griol, M. Baquero, B. Vilquin, F. Eltes, S. Abel, J. Fompeyrine, and P. Sanchis, "Barium titanate ($BaTiO_3$) RF characterization for application in electro-optic modulators," Opt. Mater. Express **7**(12), 4328 (2017).
21. G. F. Feutmba, A. Hermans, J. P. George, H. Rijckaert, I. Ansari, V. Thourhout, and J. Beeckman, "Reversible and tunable second-order nonlinear optical susceptibility in PZT thin films for integrated optics," Adv. Opt. Mater. **9**(16), 2100149 (2021).
22. T. Rutirawut, W. Talataisong, and F. Y. Gardes, "Designs of silicon nitride slot waveguide modulators with electro-optic polymer and the effect of induced charges in Si-substrate on their performance," IEEE Photonics J. **13**(2), 1–15 (2021).
23. G. Gopalakrishnan, W. Burns, R. McElhanon, C. Bulmer, and A. Greenblatt, "Performance and modeling of broadband $LiNbO/_3$ traveling wave optical intensity modulators," J. Lightwave Technol. **12**(10), 1807–1819 (1994).
24. M. Zhang, C. Wang, P. Kharel, D. Zhu, and M. Lončar, "Integrated lithium niobate electro-optic modulators: when performance meets scalability," Optica **8**(5), 652 (2021).
25. C. Svensson and G. Dermer, "Time domain modeling of lossy interconnects," IEEE Trans. Adv. Packag. **24**(2), 191–196 (2001).
26. A. Djordjevic, R. Biljie, V. Likar-Smiljanic, and T. Sarkar, "Wideband frequency-domain characterization of FR-4 and time-domain causality," IEEE Trans. Electromagn. Compat. **43**(4), 662–667 (2001).
27. G. F. Feutmba, J. P. George, K. Alexander, D. Van Thourhout, and J. Beeckman, "Hybrid PZT/Si TM/TE electro-optic phase modulators," Proc. SPIE **10921**, 109210Q (2019).

Optical Materials EXPRESS

28. H. Chung, W. Chang, and E. Adler, "Modeling and optimization of traveling-wave $LiNbO_3$ interferometric modulators," IEEE J. Quantum Electron. **27**(3), 608–617 (1991).
29. A. K. Verma, *Introduction to Modern Planar Transmission Lines: Physical, Analytical, and Circuit Models Approach* (Wiley, 2021), 1st ed.
30. M. Vanhoecke, A. Aimone, N. Argyris, S. Dris, R. Vaernewyck, K. Verheyen, M. Gruner, G. Fiol, D. Apostolopoulos, H. Avramopoulos, G. Torfs, X. Yin, and J. Bauwelinck, "Segmented optical transmitter comprising a CMOS driver array and an InP IQ-MZM for advanced modulation formats," J. Lightwave Technol. **35**(4), 862–867 (2017).
31. S. Y. Siew, B. Li, F. Gao, H. Y. Zheng, W. Zhang, P. Guo, S. W. Xie, A. Song, B. Dong, L. W. Luo, C. Li, X. Luo, and G.-Q. Lo, "Review of silicon photonics technology and platform development," J. Lightwave Technol. **39**(13), 4374–4389 (2021).